

# Characterization of Input Current Interharmonics in Adjustable Speed Drives

Hamid Soltani, *Member, IEEE*, Pooya Davari, *Member, IEEE*, Firuz Zare, *Senior Member, IEEE*, Poh Chiang Loh, and Frede Blaabjerg, *Fellow, IEEE*

**Abstract**—This paper investigates the interharmonic generation process in the input current of double-stage adjustable speed drives (ASDs) based on voltage-source inverters and front-end diode rectifiers. The effects of the inverter output-side low order harmonics, caused by implementing the double-edge symmetrical regularly sampled space vector modulation technique, on the input current interharmonic components are presented and discussed. Particular attention is also given to the influence of the asymmetrical regularly sampled modulation technique on the drive input current interharmonics. The developed theoretical analysis predicts the drive interharmonic frequency locations with respect to the selected sampling strategies. Simulation and experimental results on a 2.5 kW ASD system verify the effectiveness of the theoretical analysis.

**Index Terms**—Adjustable speed drives (ASDs), asymmetrical regularly sampling, harmonics, interharmonics, symmetrical regularly sampling, voltage source converter.

## I. INTRODUCTION

ADJUSTABLE speed drive (ASD) systems are widely used in industrial applications mainly due to less energy consumption, lower system maintenance, and also an optimum control process. Although a highly suitable performance can be achieved by employing the ASDs, at the same time they are considered as main source of harmonics and interharmonics in the grid. Fig. 1 illustrates a typical harmonic and interharmonic configuration in a double-stage voltage source inverter fed ASD. The input/output side harmonic and interharmonic distortions are shown by the solid lines, whereas the dash lines represent the associated dc-link distortions. When the inverter operates within a wide range of output frequencies, the input/output side harmonics can pass through the dc-link stage and they may consequently result in the interharmonic distortion at the input/output terminals of the ASD.

Manuscript received August 11, 2016; revised October 23, 2016; accepted December 19, 2016. Date of publication December 22, 2016; date of current version June 23, 2017. Recommended for publication by Associate Editor R. Kennel.

H. Soltani, P. Davari, and F. Blaabjerg are with the Department of Energy Technology, Aalborg University, Aalborg 9220, Denmark (e-mail: hso@et.aau.dk; pda@et.aau.dk; fbl@et.aau.dk).

F. Zare is with the Power and Energy Systems, University of Queensland, Brisbane Qld 4072, Australia (e-mail: f.zare@uq.edu.au).

P. C. Loh is with the Department of Electronic Engineering, Chinese University of Hong Kong, Hong Kong (e-mail: pcloh@ee.cuhk.edu.hk).

Color versions of one or more of the figures in this paper are available online at <http://ieeexplore.ieee.org>.

Digital Object Identifier 10.1109/TPEL.2016.2644270

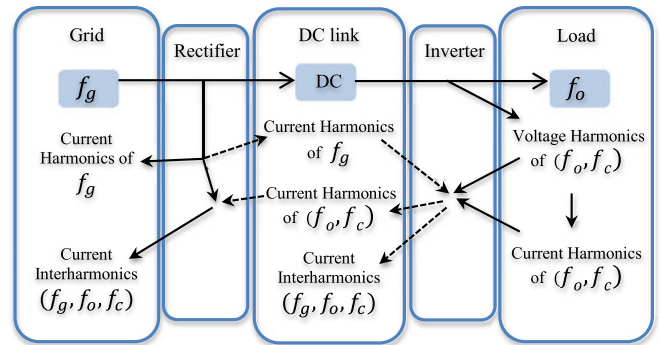


Fig. 1. Harmonic and interharmonic configuration in a double-stage ASD system [13].

Over the years, many research studies have been devoted to the analysis and investigation of harmonics [1]–[4], whereas less have been dedicated to the interharmonic issues. With the rapid growth of power electronic applications, the deteriorate effects of interharmonics are becoming more and more evident [5], [6]. Consequently, interharmonic power quality issues have gained more attention in the recent years.

Interharmonics are spectral components of voltages or currents, which are not multiple integer of the fundamental supply frequency [7]. Interharmonic extents are usually lower than those of the characteristic harmonics, but can still cause their unique effects such as light flickers, overheating of transformer, interference with control and protection signals, side-band torques exerted on the motor/generator shaft, and dormant resonance excitation [8]–[12].

Many investigations related to interharmonics have been initiated focusing more on explaining their sources, appropriate modeling, and accurate identification and detection methods [14]–[21]. Meanwhile, the amplitude and frequency analysis of interharmonics are considered to be the major subjects of interest. The precise analysis of interharmonic amplitudes is difficult, especially realizing that different real-world factors such as the grid background distortion and the converter nonlinearities may affect the drive interharmonic performance. Nevertheless, evaluation of the interharmonic amplitudes needs to be performed in all operating conditions of the ASD [22], [23]. In this respect, some investigations are also devoted to the analysis of the drive input current interharmonics by considering the motor-side current imbalance and the grid-side background distortion [12], [24], [25]. The interharmonic frequency

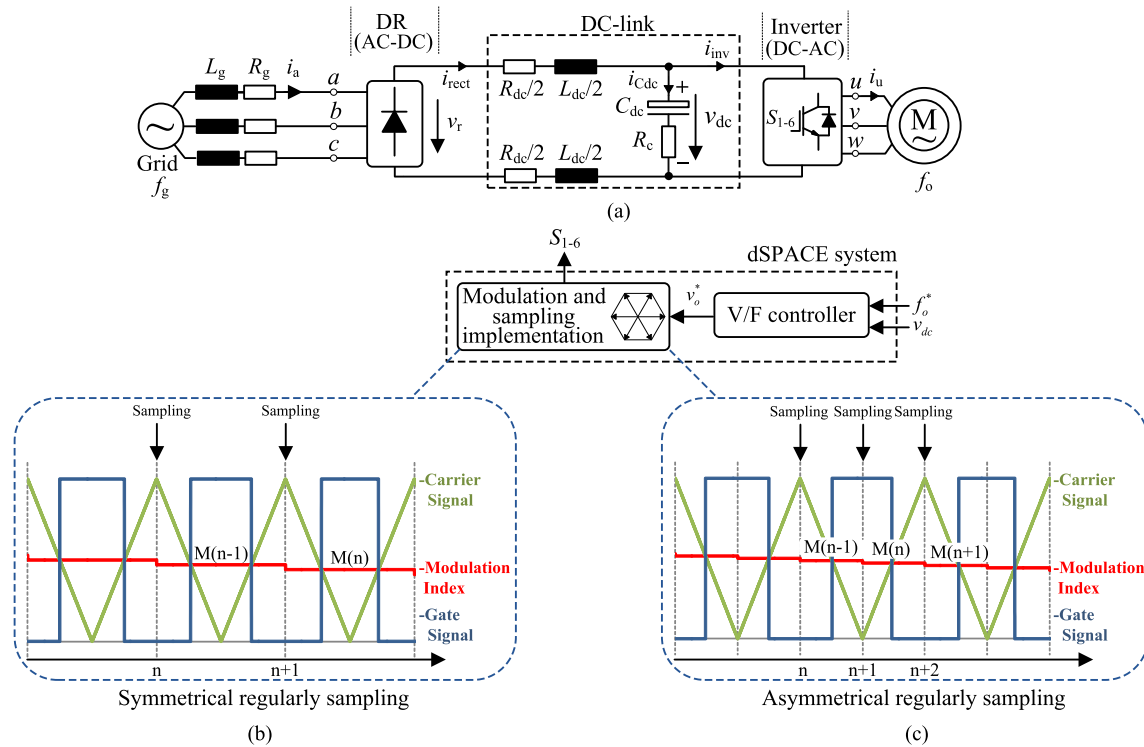


Fig. 2. Schematics of an ASD with the control and sampling units. (a) Equivalent circuit diagram of the ASD with an Induction Motor (IM); (b) The symmetrical regularly sampled modulation strategy with the corresponding gate signal; and (c) The asymmetrical regularly sampled modulation strategy with the corresponding gate signal.

evaluation has also been of highly importance, where it has initiated a lot of research works focusing on their origins [12], [26], [27]. By knowing the interharmonic locations in advance, an optimal operating strategy can be adopted to avoid the undesirable consequences.

The interharmonic generation process of the double-stage ASD has been studied in [26], where a naturally sampled sinusoidal pulse width modulation technique has been chosen for the inverter at relatively low switching frequency. The theoretical analysis was realized to provide a good understanding of the harmonic interactions, and consequently to assess the interharmonics. However, more attention is needed to precisely analyze the ASD interharmonic frequencies in practical applications.

In a digital implementation of the pulse width modulation techniques, it is difficult to apply the naturally sampled modulation strategy due to its complexity. Instead, the regularly sampled modulation strategies, symmetrical and asymmetrical, which can be easily implemented digitally are selected as the most appropriate modulation methods. In addition, the literature studies show the better performance of asymmetrical regularly sampled modulation technique compared with the symmetrical one from a harmonic point of view [28]. In this regard, the effects of regularly sampled symmetrical and asymmetrical modulation strategies on the ASD interharmonic frequency locations can be subjected to further investigation.

The main aim of this paper is to characterize the ASD input current interharmonic frequencies, when the regularly sampled space vector modulation (SVM) technique is selected due to its superior performance especially in the ASD applications. It

shows how the inverter output side harmonics caused by the double-edge symmetrical regularly sampled SVM modulation scheme may flow into the grid and consequently may result in the drive input current interharmonic components. A frequency mapping is then derived for the interharmonic frequencies based on the ASD operating points. Moreover, the possible effects of the double-edge asymmetrical regularly sampled SVM on the interharmonic locations will be evaluated and discussed. A comparison between the symmetrical and asymmetrical strategies is made to illustrate their performances from an interharmonic perspective. The developed theoretical analysis is verified by simulation and experimental results.

## II. HARMONIC TRANSFER AT INVERTER LEVEL

In this section, the transfer of the ASD output side harmonics through the inverter stage will be investigated. The double-stage ASD system model is illustrated in Fig. 2(a). The system begins with a three-phase diode-bridge rectifier, where it rectifies the ac supply voltage and provides the desired voltage level in the dc link. The embedded dc-link filters (i.e., dc-link inductors and capacitor) will lead to a smoother current and voltage for powering the rear-end inverter. The inverter is then used to synthesize three-phase balanced voltages at the output terminals with an arbitrary frequency  $f_o$  from the dc-link voltage.

By applying a pulse width modulation strategy, where a low-frequency reference signal is compared with a high-frequency carrier signal, the switched output voltage waveforms can be obtained. Since the pulse width modulation (PWM) process does

not generally generate periodic pulsating waveforms, a double-Fourier integral approach can be applied to analytically quantify the harmonic components of the inverter output voltage. As a result, the general form of the output voltages  $v_x$  ( $x = u, v, w$ ) can be expressed as (1), with a dc component, baseband harmonics (simple harmonics of the fundamental output frequency  $f_o$ ), harmonics of the carrier frequency  $f_c$ , and carrier sidebands which are accommodated around the carrier harmonics [28]

$$v_x(t) = \frac{A_{00}}{2} + \sum_{n=1}^{\infty} \left[ A_{0n} \cos \left( n \left[ \omega_o t - p \frac{2\pi}{3} \right] \right) \right. \\ \left. + B_{0n} \sin \left( n \left[ \omega_o t - p \frac{2\pi}{3} \right] \right) \right] \\ + \sum_{m=1}^{\infty} \sum_{n=-\infty}^{\infty} \left[ A_{mn} \cos \left( m\omega_c t + n \left[ \omega_o t - p \frac{2\pi}{3} \right] \right) \right. \\ \left. + B_{mn} \sin \left( m\omega_c t + n \left[ \omega_o t - p \frac{2\pi}{3} \right] \right) \right] \quad (1)$$

with  $m$  and  $n$  variables stating the carrier index and the baseband index, respectively. The fundamental and carrier angular frequencies are also defined as  $\omega_o$  and  $\omega_c$ , respectively. The  $p$  values are 0, 1, and  $-1$  with respect to the output phases  $u$ ,  $v$ , and  $w$ . The spectral coefficients  $A_{mn}$  and  $B_{mn}$ , which are defined by a double-Fourier integral can be obtained according to the selected modulation strategy.

The PWM process is normally implemented by the three most commonly used sampling strategies; the naturally sampling, the symmetrical regularly sampling; and the asymmetrical regularly sampling strategies. In a digital implementation of a naturally sampling technique, where a pure sinusoidal reference waveform should be compared with the carrier signal, it is difficult to find the exact intersection point between the modulation and modulating signals. As a result, the regularly sampled (symmetrical and/or asymmetrical) modulation methods are mostly applied for the PWM process. The implementation strategies of the symmetrical and asymmetrical regularly sampled modulation techniques are depicted in Fig. 2(b) and (c), respectively. As it can be observed in the symmetrical case, the sampled signal during each carrier interval is used to be compared with the respected carrier waveform at the next carrier interval. As for the asymmetrical one, shown in Fig. 2(c), it can be observed that the same comparative process is performed during each half carrier interval.

The theoretical closed form solutions of the inverter average pole voltage corresponding with the double-edge regularly sampled symmetrical and asymmetrical SVM techniques can be obtained by substituting (21) and (22) as the spectral coefficients, given in the Appendix [28], into (1). Fig. 3(a) and (b) shows the inverter output voltage frequency spectrum normalized with respect to the dc-link voltage for the modulation index  $M = 0.9$  and the output frequency  $f_o = 33$  Hz. As it can be seen, applying the asymmetrical regularly sampled SVM method can give rise to less output voltage harmonics compared with the symmetrical case.

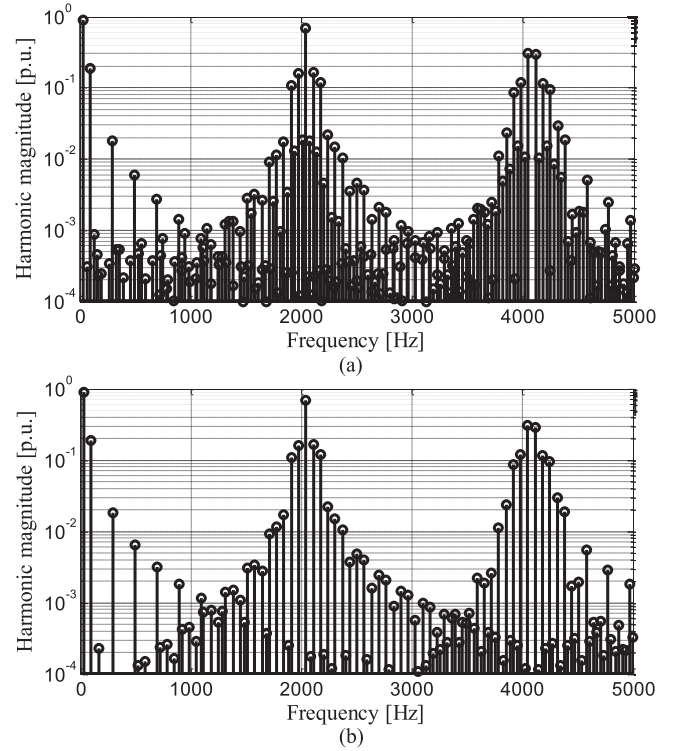


Fig. 3. Theoretical harmonic spectrum of the inverter output voltage with the modulation index  $M = 0.9$  and at the output frequency  $f_o = 33$  Hz. (a) Harmonic spectrum with symmetrical strategy [see Fig. 2(b)]. (b) Harmonic spectrum with asymmetrical strategy [see Fig. 2(c)].

By considering a highly inductive load like the Induction Motor (IM), the inverter three-phase output currents  $i_x$  ( $x = u, v, w$ ) can be assumed to be sinusoidal and they are given as

$$i_u(t) = I_o \cos(\omega_o t + \theta) \quad (2)$$

$$i_v(t) = I_o \cos \left( \omega_o t + \theta - \frac{2\pi}{3} \right) \quad (3)$$

$$i_w(t) = I_o \cos \left( \omega_o t + \theta + \frac{2\pi}{3} \right) \quad (4)$$

where the amplitude of the output currents and the displacement factor are denoted as  $I_o$  and  $\theta$ , respectively. Assuming that the inverter operates as a lossless system, with a balanced load condition, the dc-link inverter side current  $i_{inv}$  can be evaluated as

$$i_{inv}(t) = S_u(t) \cdot i_u(t) + S_v(t) \cdot i_v(t) + S_w(t) \cdot i_w(t) \quad (5)$$

where the inverter switching functions are notated as  $S_u(t)$ ,  $S_v(t)$ , and  $S_w(t)$ , and they can be defined by

$$S_x(t) = \frac{v_x(t)}{V_{dc}}, \quad x = u, v, w \quad (6)$$

the dc value of the dc-link voltage is represented as  $V_{dc}$ . Therefore, the harmonic components of the dc-link inverter side current can be found using (5) and (6).

In order to quantify the dc-link current oscillations inherited from the inverter output side, the closed form solution in (1)

can be evaluated separately in terms of the baseband harmonic components and the carrier group components. Substituting the baseband harmonic components [first summation in (1)] and (2)–(4) into (5) and (6) will give rise to (7), shown at the bottom of the page, where the associated dc-link oscillation  $i_{inv-b}$  is obtained.

As for the contribution of the carrier group harmonics of the switched output waveform on the dc-link current oscillations, the same evaluation method can be applied. By substituting the carrier group components [double summation in (1)] and (2)–(4) into (5) and (6), the corresponding dc-link oscillation  $i_{inv-c}$  is calculated as (8), shown at the bottom of the page.

The nonzero values of the harmonic coefficients  $A_{0n}$ ,  $B_{0n}$ ,  $A_{mn}$ , and  $B_{mn}$  in (7) and (8), which they should be evaluated based on the selected modulation strategy, will determine the harmonic components of the dc-link inverter side current coming from the output side. Therefore, these effects are

considered individually in the following, for the symmetrical and asymmetrical modulation methods.

#### A. Symmetrical Regularly Sampled Strategy

In respect to symmetrical regularly sampled modulation technique, the baseband harmonic coefficients  $A_{0n}$  and  $B_{0n}$  are potentially existing for all values of  $n$ , referring to (1). However, further inspection of (7) shows that only the triple multiples of the output frequency  $\omega_o$  will appear at the dc link under balanced condition. As a result, the effects of the output voltage baseband harmonic components on the dc-link current oscillation  $f_{dc-b-sym}^h$  can be obtained as

$$f_{dc-b-sym}^h = 3 \cdot k \cdot f_o, \quad k = 1, 2, 3, \dots \quad (9)$$

Here, it is worth to note that in (9), the *odd* triple multiples of the output frequency (i.e.,  $3f_o, 9f_o, \dots$ ) are caused by

$$\begin{aligned} i_{inv-b}(t) = & \sum_{n=1}^{\infty} \left[ \frac{A_{0n} I_o}{2V_{dc}} \left[ \cos((n+1)\omega_o t + \theta) + \cos((n-1)\omega_o t - \theta) \right. \right. \\ & + \cos\left((n+1)\omega_o t + \theta - (n+1)\frac{2\pi}{3}\right) + \cos\left((n-1)\omega_o t - \theta - (n-1)\frac{2\pi}{3}\right) \\ & \left. \left. + \cos\left((n+1)\omega_o t + \theta + (n+1)\frac{2\pi}{3}\right) + \cos\left((n-1)\omega_o t - \theta + (n-1)\frac{2\pi}{3}\right) \right] \right] \\ & + \frac{B_{0n} I_o}{2V_{dc}} \left[ \sin((n+1)\omega_o t + \theta) + \sin((n-1)\omega_o t - \theta) \right. \\ & + \sin\left((n+1)\omega_o t + \theta - (n+1)\frac{2\pi}{3}\right) + \sin\left((n-1)\omega_o t - \theta - (n-1)\frac{2\pi}{3}\right) \\ & \left. \left. + \sin\left((n+1)\omega_o t + \theta + (n+1)\frac{2\pi}{3}\right) + \sin\left((n-1)\omega_o t - \theta + (n-1)\frac{2\pi}{3}\right) \right] \right] \quad (7) \end{aligned}$$

$$\begin{aligned} i_{inv-c}(t) = & \sum_{m=1}^{\infty} \sum_{n=-\infty}^{\infty} \frac{A_{mn} I_o}{2V_{dc}} \left[ \cos(m\omega_c t + (n+1)\omega_o t + \theta) + \cos(m\omega_c t + (n-1)\omega_o t - \theta) \right. \\ & + \cos\left(m\omega_c t + (n+1)\omega_o t + \theta - (n+1)\frac{2\pi}{3}\right) + \cos\left(m\omega_c t + (n-1)\omega_o t - \theta - (n-1)\frac{2\pi}{3}\right) \\ & \left. \left. + \cos\left(m\omega_c t + (n+1)\omega_o t + \theta + (n+1)\frac{2\pi}{3}\right) + \cos\left(m\omega_c t + (n-1)\omega_o t - \theta + (n-1)\frac{2\pi}{3}\right) \right] \right] \\ & + \frac{B_{mn} I_o}{2V_{dc}} \left[ \sin(m\omega_c t + (n+1)\omega_o t + \theta) + \sin(m\omega_c t + (n-1)\omega_o t - \theta) \right. \\ & + \sin\left(m\omega_c t + (n+1)\omega_o t + \theta - (n+1)\frac{2\pi}{3}\right) + \sin\left(m\omega_c t + (n-1)\omega_o t - \theta - (n-1)\frac{2\pi}{3}\right) \\ & \left. \left. + \sin\left(m\omega_c t + (n+1)\omega_o t + \theta + (n+1)\frac{2\pi}{3}\right) + \sin\left(m\omega_c t + (n-1)\omega_o t - \theta + (n-1)\frac{2\pi}{3}\right) \right] \right] \quad (8) \end{aligned}$$

the corresponding *even* order baseband harmonics of the output frequency (i.e., {2th, 4th}, {8th, 10th}, ...). Moreover, the *even* triple multiples (i.e.,  $6f_o$ ,  $12f_o$ , ...) are generated by the associated *odd* order baseband harmonics of the output frequency (i.e., {5th, 7th}, {11th, 13th}, ...).

For the contribution of the carrier group harmonics, with further investigation of (8), it is found that although the carrier group coefficients  $A_{mn}$  and  $B_{mn}$  are present for all values of  $m$  and  $n$ , only the carrier harmonic components and their differences from the triple multiples of the fundamental frequency  $\omega_o$  emerge at the dc-link inverter side current. Thus, the effects of the carrier sideband harmonics on the dc-link oscillation frequencies  $f_{dc-c-sym}^h$  can be developed as

$$f_{dc-c-sym}^h = \{(m \cdot f_c), (m \cdot f_c \pm 3 \cdot k \cdot f_o)\} \quad k = 1, 2, 3, \dots \quad (10)$$

A precise investigation of (8) makes it clear that the first carrier sidebands for  $n = \pm 1$  produce the carrier frequency oscillations at the dc-link current, given in (10). Moreover, the *odd* triple sidebands of  $f_{dc-c-sym}^h$  [i.e.,  $(m \cdot f_c) - 3f_o$ ,  $(m \cdot f_c) - 9f_o$ , ...] are produced by the related *even* order sidebands of the output voltages (with the sets of  $n$  as  $\{-2, -4\}$ ,  $\{-8, -10\}$ , ...), and, the *even* triple sidebands [i.e.,  $(m \cdot f_c) - 6f_o$ ,  $(m \cdot f_c) - 12f_o$ , ...] are created by the associated *odd* order sideband carriers of the output voltages (with the sets of  $n$  as  $\{-5, -7\}$ ,  $\{-11, -13\}$ , ...).

The general expression of the dc-link inverter side current oscillations, when the symmetrical regularly sampled modulation strategy is applied, can be established by the combination of (9) and (10) as follows:

$$f_{dc-sym}^h = \{f_{dc-b-sym}^h, f_{dc-c-sym}^h\}. \quad (11)$$

### B. Asymmetrical Regularly Sampled Strategy

In the asymmetrical regularly sampled method, the baseband harmonic coefficients  $A_{0n}$  and  $B_{0n}$  are zero for *even* order harmonics [more details about these coefficients have been provided in the Appendix using (22)]. Therefore, the *odd* triple multiples of the output frequency (i.e.,  $3f_o$ ,  $9f_o$ , ...), which they were present in the case of symmetrical technique, would be removed by applying an asymmetrical modulation scheme. The contribution of the baseband harmonics on the dc-link current oscillation is then expressed as

$$f_{dc-b-asym}^h = 6 \cdot k \cdot f_o, \quad k = 1, 2, 3, \dots \quad (12)$$

In this condition, like the symmetrical case, the *even* triple multiples (i.e.,  $6f_o$ ,  $12f_o$ , ...) are made by the corresponding *odd* order baseband harmonics of the output frequency (i.e., {5th, 7th}, {11th, 13th}, ...).

As for the effect of the output voltage carrier group harmonics on the dc-link current, through examination of (22) it can be found that the carrier group coefficients  $A_{mn}$  and  $B_{mn}$  would be zero when  $\{(m+n) = \text{even value}\}$ . Afterwards, the available coefficients of  $A_{mn}$  and  $B_{mn}$  caused by all other combinations of  $m$  and  $n$  can be evaluated in (8). Further inspection of (8) using the remaining harmonic coefficients would give rise to the

dc-link current oscillation with the frequencies of  $f_{dc-c-asym}^h$

$$f_{dc-c-asym}^h = \left\{ \begin{array}{l} (m \cdot f_c \pm 3 \cdot k' \cdot f_o), \\ \quad \text{for } k' = 1, 3, 5, \dots \text{ and } m = \text{odd} \\ (m \cdot f_c), (m \cdot f_c \pm 6 \cdot k' \cdot f_o), \\ \quad \text{for } k' = 1, 2, 3, \dots \text{ and } m = \text{even} \end{array} \right\} \quad (13)$$

Consequently, the harmonic frequencies of the dc-link current by implementing the asymmetrical regularly sampled technique can be evaluated as

$$f_{dc-asym}^h = \{f_{dc-b-asym}^h, f_{dc-c-asym}^h\}. \quad (14)$$

### III. HARMONIC TRANSFER AT RECTIFIER LEVEL

The dc-link inverter side oscillations, when pass through the dc stage, encounter with the equivalent dc-link transfer function imposed by the employed passive filter components (i.e., the ac/dc chokes and the dc-link capacitor). Consequently, the oscillations amplitude would change at this stage, while their frequencies remain constant.

The dc-link inverter side current oscillations, after flowing through the dc-link stage, will be multiplied by the well-known six-pulse diode rectifier switching functions  $\{S_a(t), S_b(t), S_c(t)\}$  defined in (15)–(17), and they will make their contribution to the input currents as given in (18)

$$S_a(t) = \frac{2\sqrt{3}}{\pi} \left( \cos(\omega_g t) \pm \sum_{k=1}^{\infty} \frac{\cos[(6k \pm 1)(\omega_g t)]}{6k \pm 1} \right) \quad (15)$$

$$S_b(t) = S_a(t - T/3) \quad (16)$$

$$S_c(t) = S_a(t + T/3) \quad (17)$$

$$i_x(t) = S_x(t) \cdot i_{\text{rect}}(t) \quad x = a, b, c \quad (18)$$

where the grid voltage fundamental period and the angular frequency are notated as  $T$  and  $\omega_g$ .

As a result of the multiplication in (18), the dc-link current oscillations coming from the inverter output side will appear as the ASD input current interharmonics. The corresponding interharmonic frequencies can be written, respectively, for the symmetrical and the asymmetrical strategies, as

$$f_{ih-sym}^h = \left| [6 \cdot (\lambda - 1) \pm 1] \cdot f_g \pm f_{dc-sym}^h \right|, \quad \lambda = 1, 2, 3, \dots \quad (19)$$

$$f_{ih-asym}^h = \left| [6 \cdot (\lambda - 1) \pm 1] \cdot f_g \pm f_{dc-asym}^h \right|, \quad \lambda = 1, 2, 3, \dots \quad (20)$$

Fig. 4 shows the selected modulation strategy at the inverter, where the switching frequency is kept constant at 5 kHz during the output frequency  $f_o$  variations from 5–50 Hz. For the sake of clarification, the drive input current interharmonic locations, obtained using (19) and (20), are plotted in Fig. 5(a) and (b), only for the output frequency  $f_o$  range from 30–50 Hz. It should

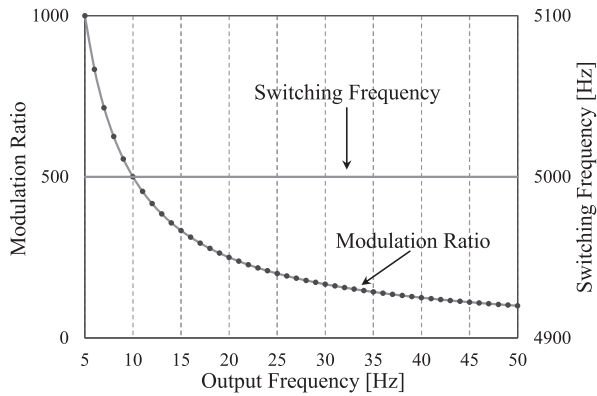


Fig. 4. Inverter switching frequency and the corresponding modulation ratio at different output frequency  $f_o$  variation ranges.

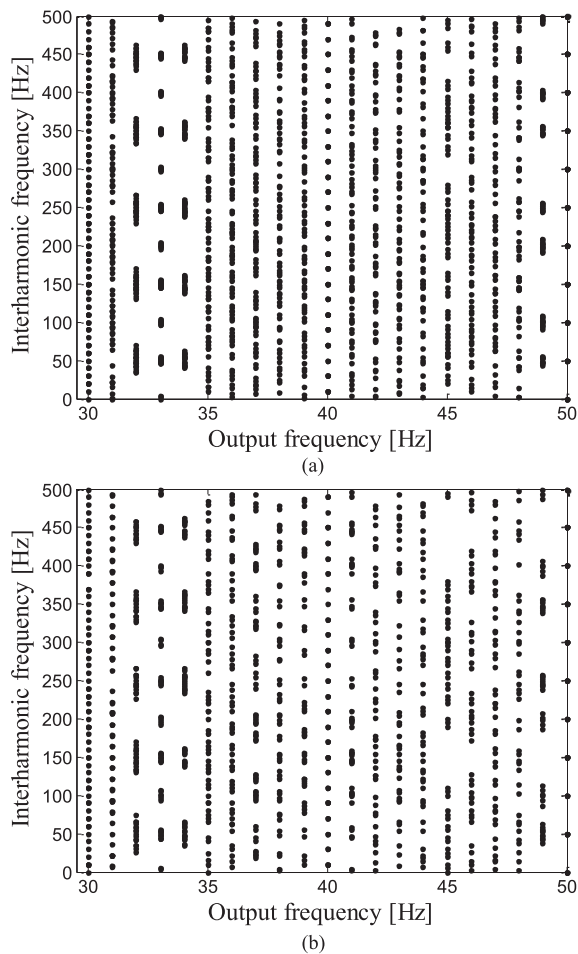


Fig. 5. ASD input current  $i_a$  interharmonic frequency locations with respect to output frequency  $f_o$  variations, (a) by applying the symmetrical modulation method, and using (19), (b) by applying the asymmetrical modulation method, and using (20).

be noted that for plotting Fig. 5, the interactions between the significant ac side harmonics (i.e., 1st, 5th, 7th, 11th, and 13th) and the dc-link current harmonics below 600 Hz coming from the inverter side have been considered.

As it can be seen in Fig. 5, the drive input current interharmonics change their locations with respect to output frequency

variations. Most interharmonic overlaps occur at the output frequencies of 33 and 50 Hz, where the interharmonics are located at the input side harmonic frequencies and/or very close to them. Based on the theoretical investigation, the asymmetrical modulation strategy may result in less interharmonic overlaps compared with the symmetrical one, and consequently it may give rise to interharmonics with different amplitudes.

#### IV. HARDWARE SETUP AND PRACTICAL IMPLEMENTATION

##### A. Hardware Setup

In order to validate the accuracy of the theoretical analysis presented in the Sections II and III, a set of simulation and experimental tests were performed in accordance to the schematic diagram shown in Fig. 6(a). The system parameter values used for MATLAB simulation and experimental work are listed in Table I. Fig. 6(b) shows the employed experimental setup. The IM is controlled with a constant voltage-to-frequency (V/F) strategy using a 2.5 kW Danfoss inverter, and the load torque was implemented by controlling a permanent magnet synchronous machine (PMSM) coupled with the IM via a 10 kW Danfoss inverter. The control algorithm was executed on a dSPACE1103 real-time platform. Moreover, a California MX30 three-phase grid simulator was used to remove the potential grid background distortion.

##### B. Measurement

It is generally well accepted that the interharmonics detection and measurements usually suffer from the spectral leakage phenomenon and the picket fence effect [29]–[31]. In this respect, it is always difficult to measure and analyze the signal's interharmonic components with acceptable levels of accuracy.

The spectral leakage can usually occur in the power system waveform analysis, due to the error in synchronizing the fundamental frequency and harmonics, and also, due to the picket fence effect normally seen for measurement of those interharmonics nonsynchronized with Discrete Fourier Transform (DFT) bins. In this condition, applying the rectangular window (RW) for the harmonic and interharmonic identification may result in an inaccurate measurement [29]. This inaccuracy is mainly induced due to the RW characterization in the frequency domain, with the narrowest main lobe, but the highest and slowly decaying side lobes.

In order to reduce the potential leakage problem during the interharmonics identification, several windowing techniques with quickly decaying side lobes can be implemented. Meanwhile, applying Hanning window is recognized as one of the most suitable choices for the harmonic and interharmonic detections, because of better side-lobe behavior compared to that of the RW [32]. The spectral characteristics of the rectangular and Hanning windows based on a 5-Hz frequency resolution are depicted in Fig. 7. In our investigations during the experimental measurement, a high accuracy DFT (with a 3-s Hanning window) [29] has been implemented for the interharmonics detection. With this choice of windowing, an approximately 0.33 Hz

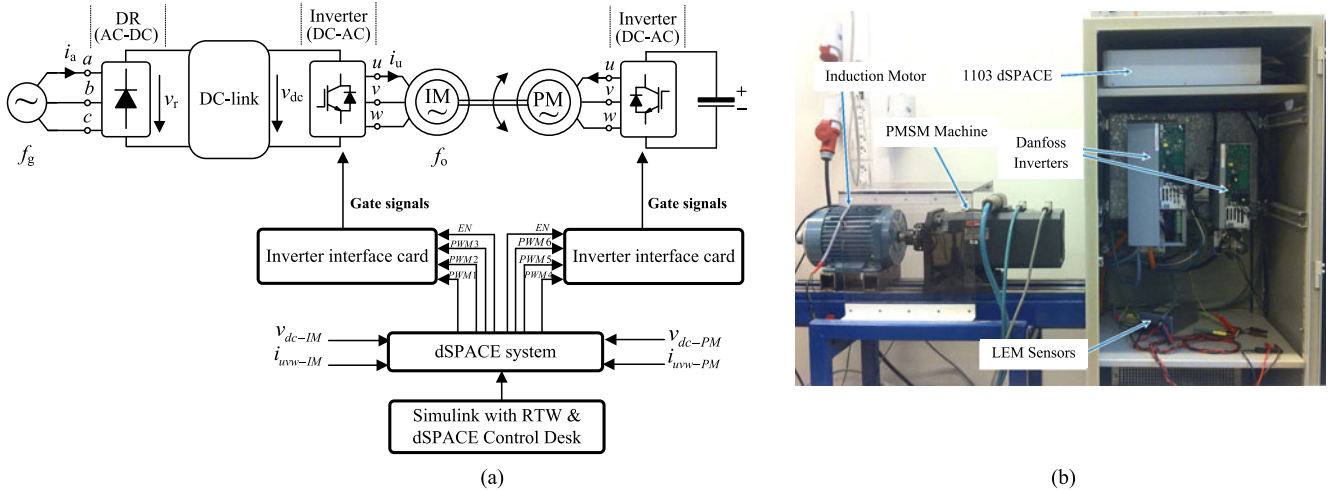


Fig. 6. Practical implementation of the ASD system; (a) Schematic of the implemented setup with an IM coupled with a permanent magnet synchronous machine (PMSM) as a load; (b) Photograph of the hardware setup.

TABLE I  
SIMULATION AND EXPERIMENTAL PARAMETERS VALUES

Symbol	Parameter	Value
$v_{a,b,c}$	Grid phase voltage	225 V <sub>rms</sub>
$f_g$	Grid frequency	50 Hz
$L_{dc}, R_{dc}$	DC-link inductor & resistor	8 mH, 360 mΩ
$C_{dc}, R_c$	DC-link Capacitor & Resistor	125 μF and 500 mΩ
$f_c$	Inverter switching frequency	5 kHz
$v_{LL}$	IM rated voltage	380 V <sub>rms</sub>
$P_{IM}$	IM rated power	2.2 kW

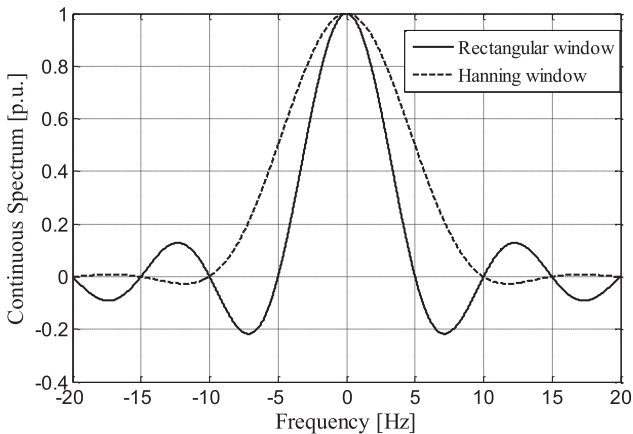


Fig. 7. Continuous spectrum of rectangular window (RW) and Hanning window (HW).

frequency resolution was obtained, and the leakage problem was minimized.

## V. SIMULATION AND LABORATORY TEST RESULTS

Fig. 8(a) and (b) show the simulated ASD output currents, the input current and voltage, and dc-link voltage waveforms, when a space vector modulation technique has been used for

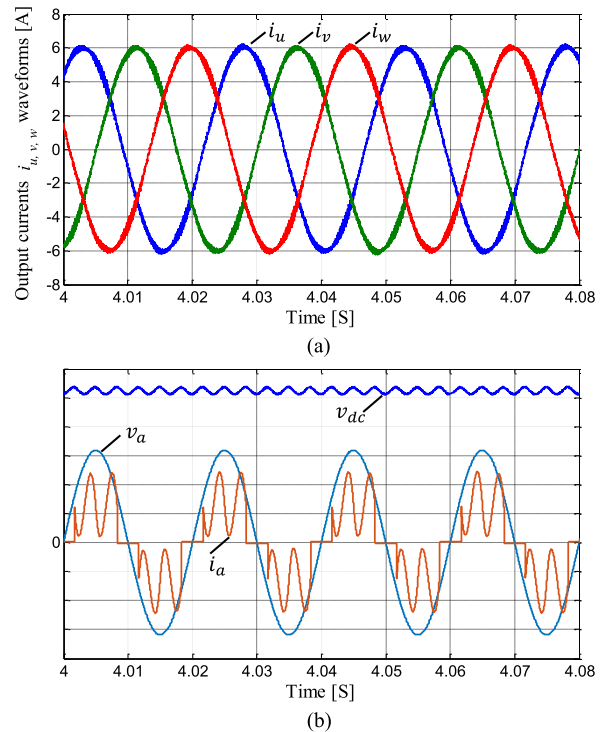


Fig. 8. (a) Simulated three-phase motor currents  $i_{u,v,w}$  waveforms. (b) The simulated input current  $i_a$  (2.5 A/div), input phase voltage  $v_a$  (100 V/div), and dc-link voltage  $v_{dc}$  (100 V/div) waveforms, when the induction motor (IM) is operating at the output frequency  $f_o = 40$  Hz and the load torque  $T_L = 12$  N · m.

the inverter operation. The IM is also set to run at the output frequency  $f_o = 40$  Hz with a load torque  $T_L = 12$  N · m. Regarding the selected (V/F) control strategy and the investigated system parameters as in Table I, the modulation index will be close to 0.818 at the output frequency  $f_o = 40$  Hz.

Fig. 9 shows the frequency evaluation of the drive input current  $i_a$ , where a symmetrical regularly sampled strategy

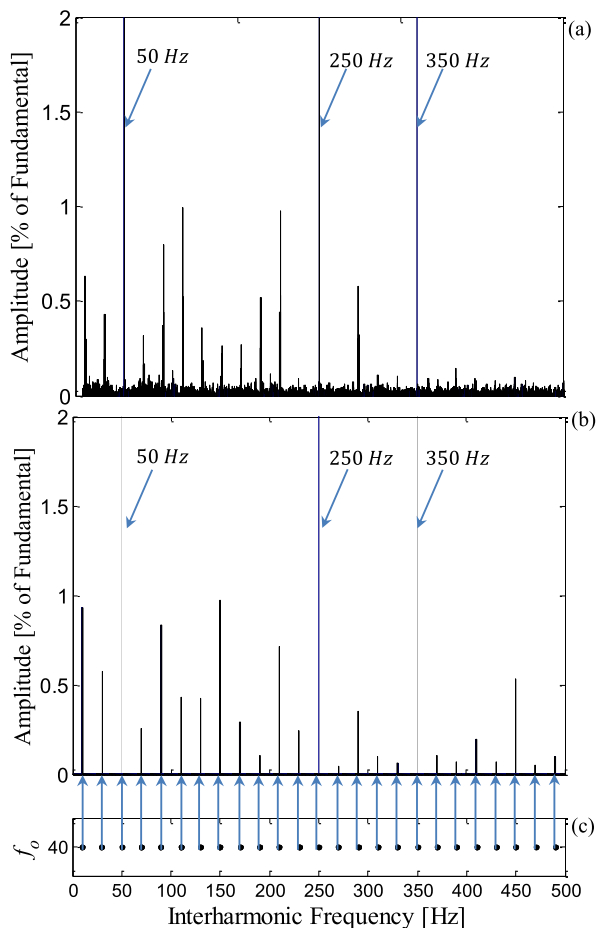


Fig. 9. Drive input current  $i_a$  interharmonics at the output frequency  $f_o = 40$  Hz and load torque  $T_L = 12$  N · m by applying a symmetrical regularly sampled SVM modulation technique: (a) Experimental result, (b) Simulation result, and (c) Output frequency versus interharmonic frequencies.

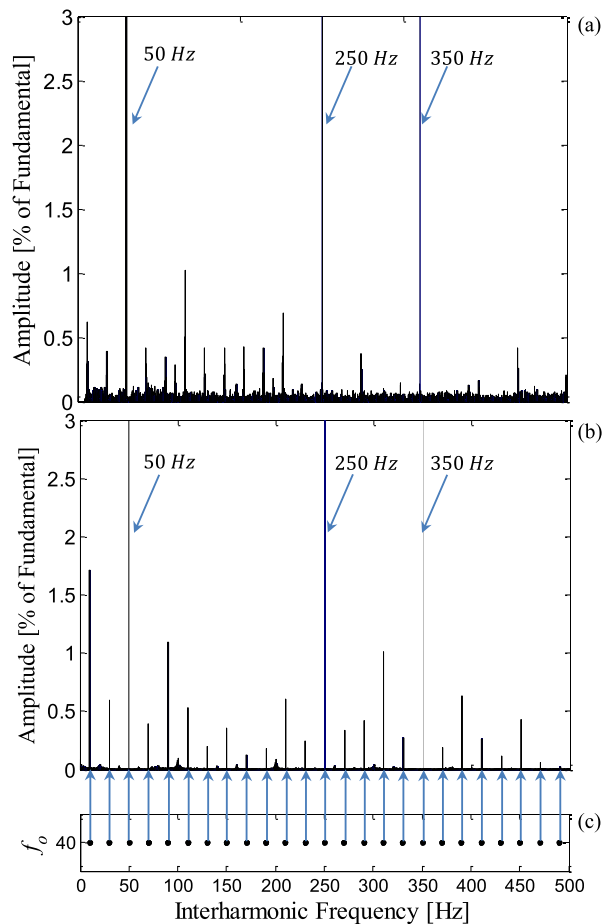


Fig. 10. Drive input current  $i_a$  interharmonics at the output frequency  $f_o = 40$  Hz and load torque  $T_L = 9$  N · m by applying a symmetrical regularly sampled SVM modulation technique: (a) Experimental result, (b) Simulation result, and (c) Output frequency versus interharmonic frequencies.

is selected at the investigated condition. The interharmonic frequency mapping, which was already obtained and shown in Fig. 5(a), is rescaled in Fig. 9(c) for further clarification. The plotted black points in Fig. 9(c) show the associated drive input current interharmonic frequencies. The frequency spectrum of the simulated drive input current  $i_a$  is depicted in Fig. 9(b), where the associated interharmonics can be observed as well as the fundamental frequency and the characteristic harmonics.

As it can be observed, the interharmonic frequency locations obtained using the theoretical analysis in (19) are in good agreement with MATLAB simulation results shown in Fig. 9(b). The frequency spectrum of the drive input current in the experimental case is illustrated in Fig. 9(a). The evaluation was next performed, when the motor operates at a load torque  $T_L = 9$  N · m with respect to the output frequency  $f_o = 40$  Hz, and the results are shown in Fig. 10. As it can be seen, the input current interharmonic frequencies obtained by the simulation and the experimental tests occur at the locations predicted by the calculation in (19). Fig. 11 shows the drive input current frequency spectrum corresponding to the output frequency  $f_o = 30$  Hz and the load torque  $T_L = 9$  N · m. The obtained experimental results, shown in Fig. 11(a), demonstrate the accuracy of the

theoretical analysis, and of the simulation results, which are shown in Fig. 11(b) and (c).

The accuracy of the theoretical analysis was also subjected to further examination in the case of applying the asymmetrical regularly sampled strategy on the inverter. Fig. 12 shows the frequency evaluation of the drive input current, when an asymmetrical method is implemented on the drive. The investigation is first performed at the output frequency  $f_o = 40$  Hz and the load torque  $T_L = 12$  N · m.

The associated theoretical frequency locations are plotted in Fig. 12(c). It is worthwhile to mention that, theoretically, the asymmetrical modulation method may give rise to less interharmonic overlaps compared with the symmetrical one, which consequently may lead to a different pattern in respect to the interharmonic amplitudes and frequencies at the same operating condition. The frequency spectrum of the simulated drive input current is depicted in Fig. 12(b), where the interharmonic components are well accommodated at the expected locations. The experimental results shown in Fig. 12(a) verifies the validity of the theoretical calculations and the simulation results.

Finally, the results associated with the asymmetrical regularly sampled modulation technique, when the motor operates

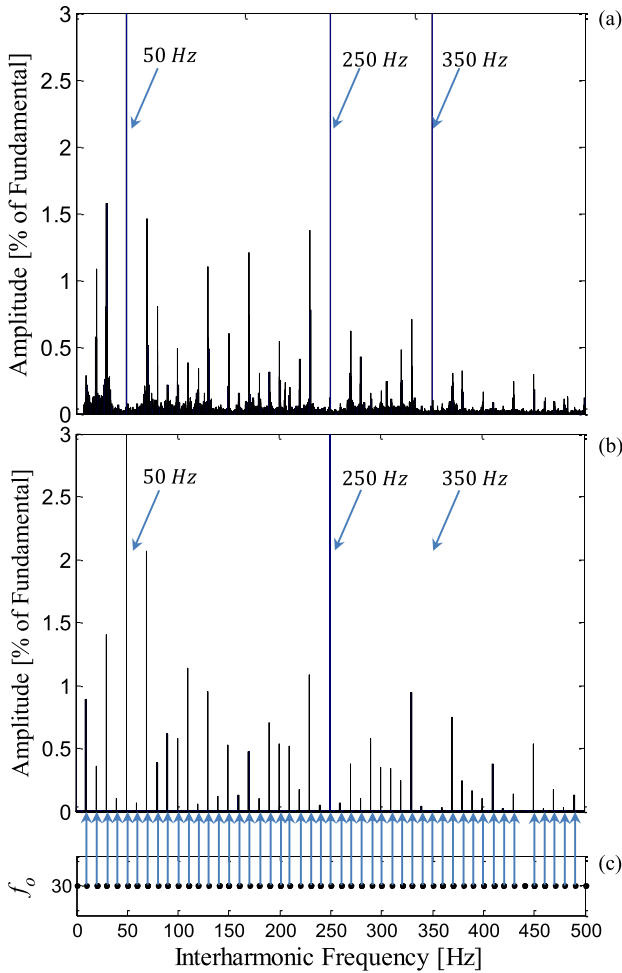


Fig. 11. Drive input current  $i_a$  interharmonics at the output frequency  $f_o = 30$  Hz and load torque  $T_L = 9$  N·m by applying a symmetrical regularly sampled SVM modulation technique: (a) Experimental result, (b) Simulation result, and (c) Output frequency versus interharmonic frequencies.

at the output frequencies of 30 and 40 Hz, with the load torque  $T_L = 9$  N·m are shown in Fig. 13. As it can be seen, a better interharmonic distortion may be obtained by implementing the asymmetrical strategy due to less interharmonic overlaps in comparison with the symmetrical modulation technique.

Notably, it is well accepted that the real-world issues (e.g., the slightly load current imbalance, the motor shaft eccentricity, the passive components degradation, and the switching non-linearity) may easily result in interharmonic components with specific frequency, or, may simply affect the interharmonics magnitude. Consequently, this phenomenon should be investigated separately depending on each application. However, the investigations in the drive input current interharmonics show that by applying the asymmetrical modulation technique, less overlaps of interharmonics will occur compared with the symmetrical one. As a result, selecting an asymmetrical modulation scheme may give rise to interharmonics with lower amplitude.

Based on Figs. 9–12, it can be observed that there are some deviations between the simulation and the experimental results with respect to the interharmonic amplitudes. In the

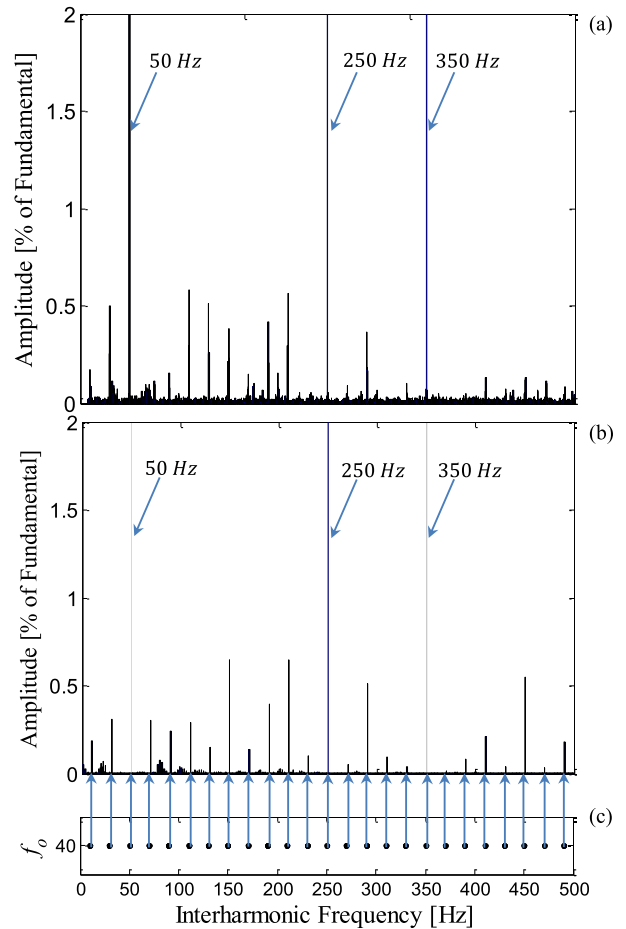


Fig. 12. Drive input current  $i_a$  interharmonics at the output frequency  $f_o = 40$  Hz and load torque  $T_L = 12$  N·m by applying an asymmetrical regularly sampled SVM modulation technique: (a) Experimental result, (b) Simulation result, and (c) Output frequency versus interharmonic frequencies.

simulation model, the switching transient and the protection algorithm effects such as the blanking time could not be implemented as the experimental case. These issues can affect the current and the voltage waveforms and consequently the overall error between the simulation and the test results.

## VI. CONCLUSION

This paper characterizes the input current interharmonics of double-stage ASDs, where the effects of the symmetrical and asymmetrical regularly sampled SVM modulation techniques are studied. A theoretical analysis has been developed for the investigated sampling strategies. The harmonic transfer from the output side of the rear-end inverter to the input side of the front-end diode rectifier has been analyzed with respect to the baseband harmonics and the carrier sideband harmonics separately. Then, the drive input current interharmonic frequencies have been plotted using the proposed analysis. Finally, the results obtained by MATLAB simulation and experimental tests demonstrate the accuracy of the analytical calculations. The investigation provides a precise benchmark for

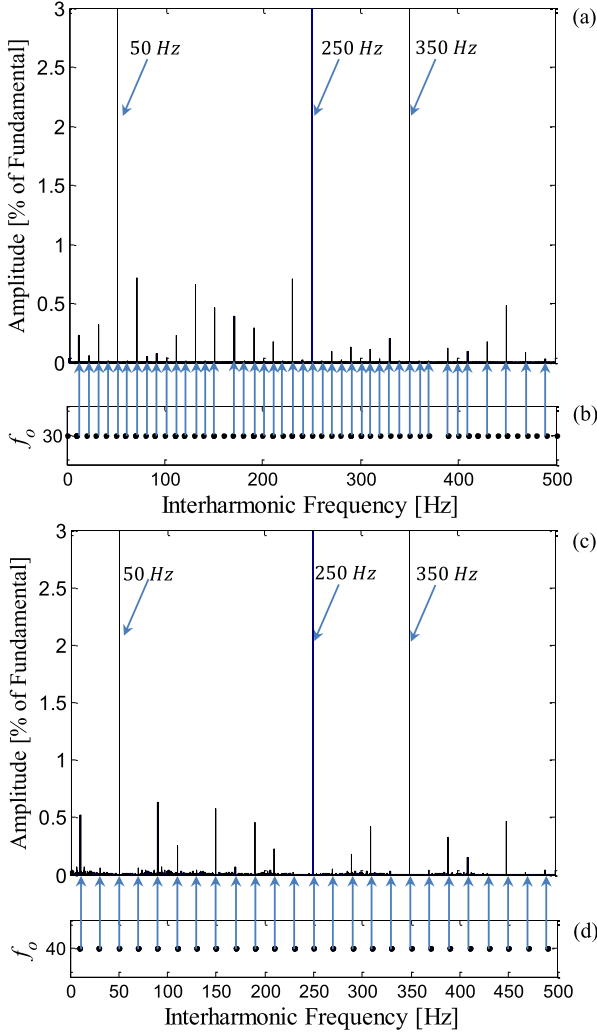


Fig. 13. Drive input current  $i_a$  interharmonics by applying an asymmetrical regularly sampled SVM modulation technique: (a) Simulation results at the output frequency  $f_o = 30$  Hz and load torque  $T_L = 9$  N · m , (b) Output frequency  $f_o = 30$  Hz versus interharmonic frequencies, (c) Simulation results at the output frequency  $f_o = 40$  Hz and load torque  $T_L = 9$  N · m, and (d) Output frequency  $f_o = 40$  Hz versus interharmonic frequencies.

estimating the ASD input current interharmonic frequencies, which also helps to choose the correct frequency resolution for the DFT spectrum analysis. Moreover according to this research, applying the asymmetrical sampling strategy may give rise to lower-amplitude interharmonics compared to the symmetrical sampling method.

#### APPENDIX

The harmonic coefficients  $A_{0n}$ ,  $B_{0n}$ ,  $A_{mn}$ , and  $B_{mn}$  in (1) can be evaluated using the double-Fourier integral. The closed form theoretical harmonic solution for the double-edge symmetrical and asymmetrical regularly sampled SVM modulation techniques are given in (21) and (22), respectively, where  $q = m + n(\omega_o/\omega_c)$ . The coefficients in (21) and (22) contain  $J_y(z)$ , which represents the Bessel functions of the first kind of

the order  $y$  and argument  $z$

$$A_{mn} + jB_{mn} = \frac{8V_{dc}}{q\pi^2} \left( \begin{aligned} & \frac{\pi}{6} \sin\left([q+n]\frac{\pi}{2}\right) \left( J_n\left(q\frac{3\pi}{4}M\right) \right. \\ & \left. + 2 \cos\left(n\frac{\pi}{6}\right) J_n\left(q\frac{\sqrt{3}\pi}{4}M\right) \right) \\ & + \frac{1}{n} \sin\left(q\frac{\pi}{2}\right) \cos\left(n\frac{\pi}{2}\right) \sin\left(n\frac{\pi}{6}\right) \left( J_0\left(q\frac{3\pi}{4}M\right) \right. \\ & \left. - J_0\left(q\frac{\sqrt{3}\pi}{4}M\right) \right) |n \neq 0 \\ & + \sum_{\substack{k=1 \\ k \neq -n}}^{\infty} \left[ \frac{1}{n+k} \sin\left([q+k]\frac{\pi}{2}\right) \cos\left([n+k]\frac{\pi}{2}\right) \right. \\ & \times \sin\left([n+k]\frac{\pi}{6}\right) \left( J_k\left(q\frac{3\pi}{4}M\right) \right. \\ & \left. + 2 \cos\left([2n+3k]\frac{\pi}{6}\right) J_k\left(q\frac{\sqrt{3}\pi}{4}M\right) \right) \\ & \left. + \sum_{\substack{k=1 \\ k \neq n}}^{\infty} \left[ \frac{1}{n-k} \sin\left([q+k]\frac{\pi}{2}\right) \cos\left([n-k]\frac{\pi}{2}\right) \right. \right. \\ & \times \sin\left([n-k]\frac{\pi}{6}\right) \\ & \left. \left( J_k\left(q\frac{3\pi}{4}M\right) + 2 \cos\left([2n-3k]\frac{\pi}{6}\right) \right. \right. \\ & \left. \left. \times J_k\left(q\frac{\sqrt{3}\pi}{4}M\right) \right) \right] \end{aligned} \right) \quad (21)$$

$$A_{mn} + jB_{mn} = \frac{8V_{dc}}{q\pi^2} \left( \begin{aligned} & \frac{\pi}{6} \sin\left([m+n]\frac{\pi}{2}\right) \left( J_n\left(q\frac{3\pi}{4}M\right) \right. \\ & \left. + 2 \cos\left(n\frac{\pi}{6}\right) J_n\left(q\frac{\sqrt{3}\pi}{4}M\right) \right) \\ & + \frac{1}{n} \sin\left(m\frac{\pi}{2}\right) \cos\left(n\frac{\pi}{2}\right) \sin\left(n\frac{\pi}{6}\right) \left( J_0\left(q\frac{3\pi}{4}M\right) \right. \\ & \left. - J_0\left(q\frac{\sqrt{3}\pi}{4}M\right) \right) |n \neq 0 \\ & + \sum_{\substack{k=1 \\ k \neq -n}}^{\infty} \left[ \frac{1}{n+k} \sin\left([m+k]\frac{\pi}{2}\right) \cos\left([n+k]\frac{\pi}{2}\right) \right. \\ & \times \sin\left([n+k]\frac{\pi}{6}\right) \\ & \quad \times \left( J_k\left(q\frac{3\pi}{4}M\right) + 2 \cos\left([2n+3k]\frac{\pi}{6}\right) \right. \\ & \quad \left. \times J_k\left(q\frac{\sqrt{3}\pi}{4}M\right) \right) \\ & \left. + \sum_{\substack{k=1 \\ k \neq n}}^{\infty} \left[ \frac{1}{n-k} \sin\left([m+k]\frac{\pi}{2}\right) \cos\left([n-k]\frac{\pi}{2}\right) \right. \right. \\ & \times \sin\left([n-k]\frac{\pi}{6}\right) \\ & \left. \left( J_k\left(q\frac{3\pi}{4}M\right) + 2 \cos\left([2n-3k]\frac{\pi}{6}\right) \right. \right. \\ & \left. \left. \times J_k\left(q\frac{\sqrt{3}\pi}{4}M\right) \right) \right] \end{aligned} \right) \quad (22)$$

## REFERENCES

- [1] M. Grötzbach, T. Strasser, and L. Lorenz, "Line side harmonics of three-phase current controlled rectifiers in continuous and discontinuous operation mode," in *Proc. IEEE Elect. Power Eng. Conf.*, 1993, pp. 707–712.
- [2] D. E. Rice, "A detailed analysis of six-pulse converter harmonic currents," *IEEE Trans. Ind. Appl.*, vol. 30, no. 2, pp. 294–304, Mar./Apr. 1994.
- [3] P. Davari, F. Zare, and F. Blaabjerg, "Pulse pattern-modulated strategy for harmonic current components reduction in three-phase AC–DC converters," *IEEE Trans. Ind. Appl.*, vol. 52, no. 4, pp. 3182–3192, Jul./Aug. 2016.
- [4] Y. Yang, P. Davari, F. Zare, and F. Blaabjerg, "A DC-link modulation scheme with phase-shifted current control for harmonic cancellations in multidrive applications," *IEEE Trans. Power Electron.*, vol. 31, no. 3, pp. 1837–1840, Mar. 2016.
- [5] L. Feola, R. Langella, and A. Testa, "On the effects of unbalances, harmonics and interharmonics on PLL systems," *IEEE Trans. Instrum. Meas.*, vol. 62, no. 9, pp. 2399–2409, Sep. 2013.
- [6] L. Feola *et al.*, "On the effects of interharmonic distortion on grid connected three-phase PV inverters," in *Proc. 15th Int. Conf. Harmonics Qual. Power*, 2012, pp. 682–688.
- [7] IEEE Interharmonic TaskForce, "Interharmonics: Theory and modeling," *IEEE Trans. Power Del.*, vol. 22, no. 4, pp. 2335–2348, Oct. 2007.
- [8] D. Gallo, C. Landi, R. Langella, and A. Testa, "IEC flickermeter response to interharmonic pollution," presented at the *11th International Conference Harmonics and Quality of Power, Lake Placid, NY, USA*, 2004, pp. 489–494.
- [9] D. Gallo, R. Langella, A. Testa, and A. Emanuel, "On the effects of voltage subharmonics on power transformers: A preliminary study," presented at the *11th International Conference Harmonics and Quality of Power, Lake Placid, NY, USA*, 2004, pp. 501–506.
- [10] M. Hernes and B. Gustavsen, "Simulation of shaft vibrations due to interaction between turbine-generator train and power electronic converters at the visund oil platform," in *Proc. IEEE Power Convers. Conf.*, 2002, pp. 1381–1386.
- [11] C. Bowler, "Proposed steady-state limits for turbine-generator torsional response," in *Proc. IEEE Summer Power Meeting*, 2002, pp. 1–6.
- [12] D. Basic, "Input current interharmonics of variable-speed drives due to motor current imbalance," *IEEE Trans. Power Del.*, vol. 25, no. 4, pp. 2797–2806, Oct. 2010.
- [13] W. J. Cho, "Mitigation of harmonic and inter-harmonic effects in nonlinear power converters," Ph.D. thesis, Faculty Graduate School, Univ. Texas Austin, Austin, TX, USA, 2010.
- [14] R. Yacamini, "Power system harmonics—Part 4: Interharmonics," *Power Eng. J.*, vol. 10, no. 4, pp. 185–193, Aug. 1996.
- [15] H. Soltani, P. C. Loh, F. Blaabjerg, and F. Zare, "Sources and mitigation of interharmonics in back-to-back controllable drives," in *Proc. IEEE Elect. Power Eng.*, 2014, pp. 1–9.
- [16] E. W. Gunther, "Interharmonics in power systems," in *Proc. IEEE Power Eng. Soc. Summer Meeting*, 2001, pp. 813–817.
- [17] M. Rifai, T. H. Ortmeier, and W. J. McQuillan, "Evaluation of current interharmonics from AC drives," *IEEE Trans. Power Del.*, vol. 15, no. 3, pp. 1094–1098, Jul. 2000.
- [18] Y. Zhang and Y. W. Li, "Investigation and suppression of harmonics interaction in high-power PWM current-source motor drives," *IEEE Trans. Power Electron.*, vol. 30, no. 2, pp. 668–679, Feb. 2015.
- [19] S. Schramm, C. Sihler, J. Song-Manguelle, and P. Rotondo, "Damping torsional interharmonic effects of large drives," *IEEE Trans. Power Electron.*, vol. 25, no. 4, pp. 1090–1098, Apr. 2010.
- [20] C.-I. Chen and Y.-C. Chen, "Comparative study of harmonic and interharmonic estimation methods for stationary and time-varying signals," *IEEE Trans. Ind. Electron.*, vol. 61, no. 1, pp. 397–404, Jan. 2014.
- [21] C.-I. Chen and G. W. Chang, "An efficient Prony-based solution procedure for tracking of power system voltage variations," *IEEE Trans. Ind. Electron.*, vol. 60, no. 7, pp. 2681–2688, Jul. 2013.
- [22] H. Soltani, F. Blaabjerg, F. Zare, and P. C. Loh, "Effects of passive components on the input current interharmonics of adjustable-speed drives," *IEEE J. Emerg. Sel. Top. Power Electron.*, vol. 4, no. 1, pp. 152–161, Mar. 2016.
- [23] G. W. Chang and S. K. Chen, "An analytical approach for characterizing harmonic and interharmonic currents generated by VSI-fed adjustable speed drives," *IEEE Trans. Power Del.*, vol. 20, no. 4, pp. 2585–2593, Oct. 2005.
- [24] R. Carbone, "Analyzing voltage background distortion effects on PWM adjustable-speed drives," *IEEE Trans. Power Electron.*, vol. 19, no. 3, pp. 765–774, May 2004.
- [25] G. W. Chang, S. K. Chen, H. J. Su, and P. K. Wang, "Accurate assessment of harmonic and interharmonic currents generated by VSI-fed drives under unbalanced supply voltages," *IEEE Trans. Power Del.*, vol. 26, no. 2, pp. 1083–1091, Apr. 2011.
- [26] F. De Rosa, R. Langella, A. Sollazzo, and A. Testa, "On the interharmonic components generated by adjustable speed drives," *IEEE Trans. Power Del.*, vol. 20, no. 4, pp. 2535–2543, Oct. 2005.
- [27] H. Soltani, P. Davari, P. C. Loh, F. Blaabjerg, and F. Zare, "Input current interharmonics in adjustable speed drives caused by fixed-frequency modulation techniques," in *Proc. IEEE Appl. Power Electron. Conf. Expo.*, 2016, pp. 229–235.
- [28] D. G. Holmes and T. A. Lipo, *Pulse Width Modulation for Power Converters: Principles and Practice*, vol. 18. Hoboken, NJ, USA: Wiley, 2003.
- [29] A. Testa, D. Gallo, and R. Langella, "On the processing of harmonics and interharmonics: Using Hanning window in standard framework," *IEEE Trans. Power Del.*, vol. 19, no. 1, pp. 28–34, Jan. 2004.
- [30] D. Gallo, R. Langella, and A. Testa, "Desynchronized processing technique for harmonic and interharmonic analysis," *IEEE Trans. Power Del.*, vol. 19, no. 3, pp. 993–1001, Jul. 2004.
- [31] H. C. Lin, "Power harmonics and interharmonics measurement using recursive group-harmonic power minimizing algorithm," *IEEE Trans. Ind. Electron.*, vol. 59, no. 2, pp. 1184–1193, Feb. 2012.
- [32] F. J. Harris, "On the use of windows for harmonic analysis with the discrete Fourier transform," *Proc. IEEE*, vol. 66, no. 1, pp. 51–83, Jan. 1978.



**Hamid Soltani** (S'14–M'16) received the B.Sc. and M.Sc. degrees in electrical engineering both from the University of Mazandaran (Noushivani), Babol, Iran, in 2005 and 2008, respectively, and the Ph.D. degree in power electronics from Aalborg University, Aalborg, Denmark, in 2016.

From 2009 to 2013, he was a Lecturer with the Department of Electrical and Computer Engineering, Golestan University, Gorgan, Iran. He is currently a Postdoctoral Researcher in the Department of Energy Technology, Aalborg University, Aalborg, Denmark.

His current research interests include harmonics analysis, power quality, power electronics topologies and control.



**Pooya Davari** (S'11–M'13) received the B.Sc. and M.Sc. degrees in electronic engineering both from the University of Mazandaran (Noushivani), Babol, Iran, in 2004 and 2008, respectively, and the Ph.D. degree in power electronics from Queensland University of Technology (QUT), Brisbane, Australia, in 2013.

From 2005 to 2010, he was involved in several electronics and power electronics projects as a Development Engineer. From 2010 to 2014, he investigated and developed high-power, high-voltage power electronic systems for multidisciplinary projects, such as ultrasound application, exhaust gas emission reduction, and tissue-materials sterilization. From 2013 to 2014, he was a Lecturer with QUT. In August 2014, he joined the Department of Energy Technology, Aalborg University, Aalborg, Denmark, as a Postdoctoral Researcher, where he is currently an Assistant Professor. His current research interests include active front-end rectifiers, harmonic mitigation in adjustable-speed drives, electromagnetic interference in power electronics, high power density power electronic systems, and pulsed power applications.

Dr. Davari was awarded the research grant from the Danish Council of Independent Research (DFF-FTP) in 2015, and he is currently working as an Editor of the *International Journal of Power Electronics*.



**Firuz Zare** (S'98–M'01–SM'06) received the Ph.D. degree in power electronics from Queensland University of Technology, Brisbane, QLD, Australia, in 2002.

He has spent several years in industry as a Team Leader working on power electronics and power quality projects. He has published more than 180 journal and conference papers and technical reports in the area of Power Electronics.

Dr. Zare is an academic staff at the University of Queensland and a Task Force Leader of Active Infeed Converters within Working Group one at the IEC standardization TC77A. He is an Associate Editor of the IEEE ACCESS JOURNAL and the Editor-in-Chief of *International Journal of Power Electronics*. He has received the several awards such as an Australian Future Fellowship, the Symposium Fellowship by the Australian Academy of Technological Science, the Early Career Academic Excellence Research Award and the John Madsen Medal from Engineers Australia.



**Poh Chiang Loh** received the B.Eng. and M.Eng. degrees both from National University of Singapore, Singapore, in 1998 and 2000, respectively, and the Ph.D. degree from Monash University, Melbourne, Vic, Australia, in 2002, all in electrical engineering.

From 2013 to 2015, he was a Professor at Aalborg University, Aalborg, Denmark. Since 2015, he has been working as a Full Professor at Chinese University of Hong Kong, Hong Kong. His current interests include in power converters and their grid applications.



**Frede Blaabjerg** (S'86–M'88–SM'97–F'03) was with ABB-Scandia, Randers, Denmark, from 1987 to 1988. He received the Ph.D. degree in electrical engineering from Aalborg University, Aalborg, Denmark, in 1992.

He became an Assistant Professor in 1992, an Associate Professor, in 1996, and a Full Professor of power electronics and drives, in 1998, Aalborg University. His current research interests include power electronics and its applications such as in wind turbines, PV systems, reliability, harmonics, and adjustable speed drives.

Dr. Blaabjerg received 15 IEEE Prize Paper Awards, the IEEE PELS Distinguished Service Award in 2009, the EPE-PEMC Council Award in 2010, the IEEE William E. Newell Power Electronics Award 2014, and the Villum Kann Rasmussen Research Award 2014. He was an Editor-in-Chief of the IEEE TRANSACTIONS ON POWER ELECTRONICS from 2006 to 2012. He has been a Distinguished Lecturer for the IEEE Power Electronics Society from 2005 to 2007 and for the IEEE Industry Applications Society from 2010 to 2011. He was nominated in 2014 by Thomson Reuters to be between the most 250 cited researchers in engineering in the world.